Non-Destructive Evaluation and Damage Determination of Fiber-Reinforced Composites by Digital Image Correlation
Hliva V., Szebényi G.

Non-Destructive Evaluation and Damage Determination of Fiber-Reinforced Composites by Digital Image Correlation

V. Hliva[1,2] · G. Szebényi[1,3]

Abstract

The trend in recent years shows that fiber-reinforced polymer composites (FRPCs) are steadily replacing traditional engineering materials in the aerospace, automotive, and sports equipment industries, where the safety and reliability of structures are of crucial importance. The increasing popularity of FRPCs is explained by their favorable mechanical properties. However, a serious problem of FRPCs is their catastrophic failure under overload and lack of ductile behavior. This issue makes it necessary to develop a non-destructive examination method that can estimate the structural integrity and predict the remaining properties of a composite structure even after its partial damage. In this paper, we propose a Digital Image Correlation (DIC)-based new method, which is able to meet all the requirements of Industry 4.0, thus this method can be automated, is fast, accurate, and excludes the human factor. To prove the efficiency of the proposed, Non-Destructive (NDT)-DIC method, we created specimens with known impact damage, and tested them firstly by infrared thermography to get a basic reference to compare the subsequent results. Then we performed the NDT-DIC tests, where through the practical example, we presented the steps and the logical deduction of the method. Firstly, the test load limit is determined, proven by AE testing to be in the non-destructive range for the examined composite system. In the case of a simple tensile test setup, the obtained result is the principal strain field from which we calculate our indicator, the X value. The X value can indicate the existence of damage by itself, furthermore, a correlation can be established that defines the X value's relationship with the reduction of strength, based on preliminary experiments. The use of the correlation enables a higher level of health monitoring than the use of the DIC method without this information because the effect of a random impact damage is predictable for the given composite. In our case, the correlation is already strong with a 0.1% strain/elongation test load, but when the test load is increased to 0.15%, the coefficient of determination (R^2) slightly increases from 0.979 to 0.997.

Keywords Fiber reinforced polymer composite (FRPC) · Barely visible impact damage (BVID) · Non-destructive evaluation (NDE) · Digital image correlation (DIC)

1 Introduction

The goal of any company is to increase its sales and profit. To achieve this in the transportation sector, companies have to develop vehicles that are more efficient, safer for passengers and drivers, and more environmentally friendly than their competitors. Nowadays, to achieve all these requirements, vehicle producers need to create high-performance structures, for which it is not enough to use traditional engineering materials such as metals or plastics. High strength-to-mass and stiffness-to-mass ratios of polymer composites, together with the tailor-made anisotropy of their properties, can ensure superiority. Furthermore, the recent progress in composite production technologies opens up new possibilities in product design. Besides the certain advantages of composites, these materials have a serious disadvantage that hinders their widespread application in vehicle structures. Unlike metals, FRPCs can exhibit sudden and catastrophic failure in the case of overload. Moreover, imperfections from production and failures accumulated during operation can decrease

✉ G. Szebényi
szebenyi@pt.bme.hu

1   Department of Polymer Engineering, Faculty of Mechanical Engineering, Budapest University of Technology and Economics, Müegyetem rkp. 3, Budapest H-1111, Hungary

2   MTA–BME Research Group for Composite Science and Technology, Müegyetem rkp. 3, Budapest H-1111, Hungary

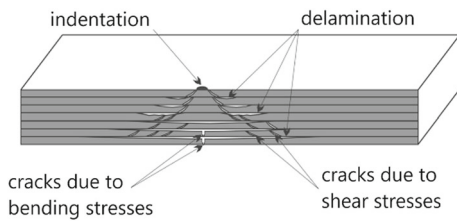3   MTA-BME Lendület Lightweight Polymer Composites Research Group, Müegyetem rkp. 3, Budapest H-1111, Hungary

Fig. 1 Typical BVID damage [6]

the structure's maximum load capacity, which was predetermined in the design stage. These defects originate from various failure modes co-occurring in the layered structure, such as matrix crack, matrix-fiber debonding, fiber rupture, and delamination [1]. For example, a typical phenomenon occurring in FRPCs is barely visible impact damage (BVID), usually caused by hits during operation. During the typical BVID, the damage in the outer surface of FRPC can hardly be identified, while, in fact, the damage inside the structure can be much more serious. Thus, the defect continuously grows in a conic or inverse conic shape from the place of impact across the thickness of the structure (Fig. 1), depending on the laminate thickness. This can cause delamination, fiber breakage, and unwanted shear stress inside the FRPC. All these internal defects can significantly reduce the load-bearing capacity of a structure even though, visually, the structure is intact [2]. The complex character of FRPC failure makes lifetime prediction difficult or even impossible [3, 4]. However, this is unacceptable in a safety–critical application [5].

To solve the problem of a catastrophic failure of composites, engineers currently apply high safety factors in design, but it increases the weight and price of the product. Another solution to avoid catastrophic failure is to increase the toughness of the FRPC. Higher toughness can be achieved in different ways. For example, the addition of nano-modifiers to the polymer matrix [7–9], hybridization for pseudo-ductility [10, 11], or modification of the interface between layers [12–15]. Increasing the toughness of composites is a hot topic nowadays. Although several great results have been achieved, the problem of predicting the lifetime of composite structures remains. When the load reaches the point when these extra mechanisms start to work, the structure has already suffered irreversible damage. After this point, replacing the damaged part is essential, which can be expensive and time-consuming in many cases.

Another possibility to prevent catastrophic failure is the application of self-healing FRPC. Although self-healing technology has greatly improved in recent years, there are no examples of their industrial application yet. To take the next steps toward commercialization, standardization of manufacture, characterization and validation are required. Combining self-healing with structural health monitoring (SHM) may present one solution to this [16–18].
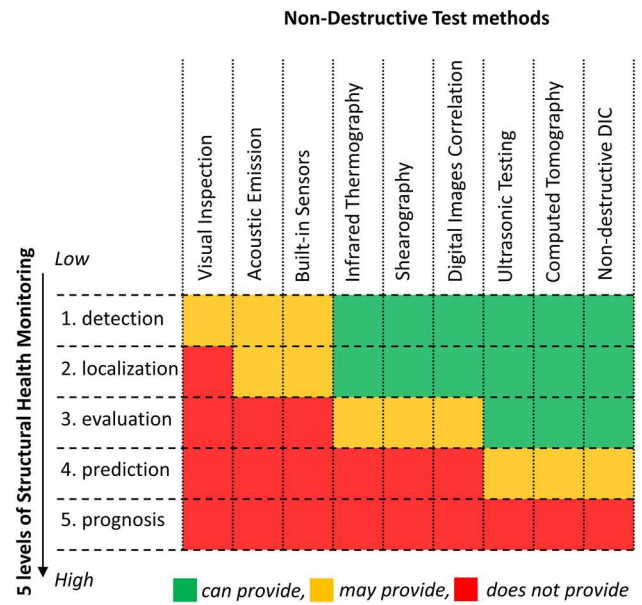

Fig. 2 Classification of test methods based on which level of SHM they can provide about barely visible impact damage

However, the structural health monitoring in itself can be a solution for the catastrophic failure issue. SHM is a complex interdisciplinary field of material, mechanical and computation science, and electronics. We can distinguish five levels of SHM based on the information that it can provide. At the first level, SHM answers the following question: Is there any detectable damage in the structure? The second level of SHM can specify the position and the dimensions of the damage in the structure. The third level provides an evaluation of the damage in the structure, the fourth gives a prediction of the lifetime of the structure, and finally, the fifth level provides a prognosis of structural damage. Reaching this fifth level is the final goal of the development of non-destructive test (NDT) methods [5, 19].

There are many options for classification methods of SHM [20, 21], for example, the working mechanism of the method, the time of the test, the price of the equipment, the location of the sensors, etc. However, in this paper, we classify the common NDT test methods depending on what level of SHM (Fig. 2) they provide about BVID.

Visual inspection is a common method of quality control. It is done by the senses (sight and touch), and good lighting and possibly a magnifier are needed. Smaller companies in the composite industry use it because its inexpensive, fast, and flexible. To avoid the human factor in mass production, big companies replace humans and use cameras or lasers on robot arms [22]. However, in the case of BVID, visual inspection is not an option—the inspector can recognize an indentation mark on the surface of a composite product but the internal damage stays hidden.

The acoustic emission (AE) testing method detects and monitors the release of stress waves from localized sources when a material deforms under stress. Such sources can be matrix fractures or fiber ruptures in a composite [23]. AE is considered non-destructive as installing microphones to record signals and data collection does not damage the structure. However, AE can only detect damage that forms or evolves during monitoring. This means AE cannot identify the defects that exist but do not progress at the moment of monitoring. Using multiple microphones, the location of the damage can be detected based on the speed of sound propagation in the material, but it does not provide information on the size and location of the damage between layers [24]. AE has been a hot topic in the last couple of decades. There are papers reporting the possibility of using AE for a higher level of SHM [25, 26]

Similar to AE, continuous monitoring is feasible with built-in sensors. Usually, the photometric or electrical properties of the fibers are exploited. A change in the measured value shows a deviation from the initial state, which can indicate a dangerous load on the structure or incipient damage. Optical fibers or fiber Bragg grating sensors (FBGs) [27] or the fibers of reinforcement [28–31] can provide internal strain information and can possibly be used for SHM. However, built-in sensors have shortcomings. First of all, to detect the BVID, they should be close to the damage, but usually, they cannot provide more information than level 2 SHM. The second problem is that if the position of damage is known, the structure cannot be repaired with the sensor kept intact.

Other NDT methods that use optical systems, like Infrared thermography (IRT), shearography, and the method that we focus on—digital image correlation (DIC) are free from this drawback [1]. These methods also offer both continuous monitoring and periodic inspection [32]. The common aspect of periodic testing methods is that they apply various kinds of excitation to the object and then measure the response. If the reaction deviates from what is expected based on calculations or from the reference, it indicates a defect. The difference between the above-mentioned methods is obviously in the type of excitation and the measured quantity. IRT detects radiation in the infrared range. Shearography uses a laser to create a speckle pattern on the surface and analyzes the obtained interference caused by a load. DIC also requires a random surface pattern, but it is usually made by black and white paint marks. This pattern changes under the influence of mechanical excitation. The strains on the surface are calculated by the algorithm from patterns of the different load steps. Several studies demonstrate that these three methods can be suitable for the detection of BVID under appropriate conditions. However, at the moment, these methods can only provide the information corresponding to the second level of SHM, although they are continuously developed.

To reach the third level of SHM, the application of a more powerful method is necessary. Computer tomography (CT) emits X-rays across the object during its rotation. CT delivers the results in the form of a detailed 3D-map of the examined part, which can provide a deep understanding of structural integrity. However, the resolution of CT decreases as the size of the examined part increases. Using CT to examine composite materials can be difficult, as composites have a higher attenuation coefficient compared to metals, which causes lower contrast between intact and damaged parts. Moreover, the CT equipment is stationary, rather expensive, and offers a relatively small test area, which hinders its widespread use. Instead of dangerous radiation, the ultrasonic test (UT) measures the reflection, transmission, or backscattering of pulsed elastic waves in the tested composite structure. The equipment is practical and easy to carry, which facilitates the mapping of BVID. The severity of the damage can be estimated from the dimensions of the damage and its position between the layers. But surface accessibility is generally required, and flaws parallel to the sound wave might not be found. Small and thin materials are also difficult to inspect with UT [33]. Wronkowicz et al. [6] developed algorithms for BVID reconstruction, which use the results of ultrasonic and X-ray computed tomographic testing. Their advanced image processing algorithms offer a significant improvement in the detectability of BVID in the tested structures compared to raw results from tests, and these also offer a better understanding of BVID for operators of NDT. Ultrasonic-guided waves-based SHM method has also been profoundly investigated for NDT of composite structures. This technique is especially suitable for SHM of composite pipes [34]. However, for monitoring flat composite structures this technique may need distributed sensor networks [35].

Based on this summary, current NDT methods can hardly provide accurate information for the next levels of SHM. However, by evaluating the results, an experienced professional may be able to give an estimate of the condition of the structure supported by standard measurements and numerical validation. Nevertheless, it is striking that there isn't a fast and flexible method that is also usable for testing large surfaces and provides information for SHM level 3 or above. To address this problem, we aimed to develop one of the non-contact optical systems to the next level of SHM. We cannot use thermomechanical load and infrared thermography or integrated optical fibers to predict residual mechanical properties after damage. The excitation and the response of the object should be mechanical and needs to be imported into the finite element analysis (FEA) software. DIC seems to be the most practical method to satisfy these needs. Due to the explosive growth of computer processing capacity in recent years, there are new opportunities to be exploited. Gomes et al. [19] presented a new algorithm to determine the location and dimension of structural damage in carbon fiber reinforced
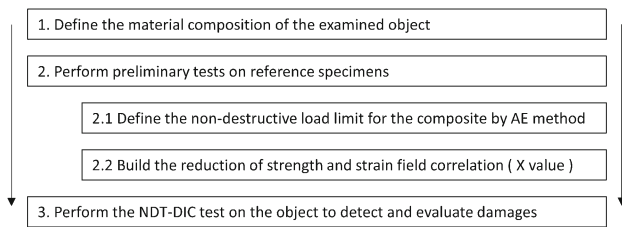
1. Define the material composition of the examined object

2. Perform preliminary tests on reference specimens

   2.1 Define the non-destructive load limit for the composite by AE method

   2.2 Build the reduction of strength and strain field correlation (X value)

3. Perform the NDT-DIC test on the object to detect and evaluate damages

Fig. 3 The general flowchart of the proposed NDT-DIC method

Table 1 Steps of experiments in a chronological order

No	Experimental plan
1	Preparation of specimens
2	DIC stage 1: NDT of 80 mm width specimens
3	IRT examination
4	DIC stage 2 + AE: NDT of 25 mm width specimens
5	DIC stage 3 + AE: tensile test
6	Post-processing

plastic (CFRP) from a strain field obtained by DIC. In another study, Khechai et al. [36] examined the strength degradation of various notched composite specimens based on the strain maps from DIC. They also investigated a stress concentration factor and failure process and compared the DIC results with the prediction of FEA. They proved that compared to experimental data, the accuracy of the predicted strength was within 17%.

Even though a lot of publications are dedicated to the research of the non-contact DIC method for damage monitoring, most of them are not non-destructive tests as during the experiment the damage in the specimens is progressing, and testing often ends at specimen failure. Such an approach is acceptable for the analysis of failure and identification of remaining properties of examined materials. By contrast, in this paper, we focus on the non-destructive way of damage detection and evaluation. The proposed NDT-DIC method can be used in these cases, when damaging the examined object is unacceptable, for example, inline quality control, or in industries, where periodic non-destructive tests are required to prevent failure. In these cases, the material composition is known, which allows making preliminary tests on specimens for the definition of a non-destructive test load level and a damage-strain field correlation. The basic steps of the NDT-DIC method are presented in Fig. 3. In our previous study [37], we presented the load level definition for the NDT-DIC method. In this study, we focus on finding the correlation between the damage and the strain field in a certain composite structure. For this, we introduce an indicator (X value) which can be useful for decision-making after the non-destructive test, if the tested part should be replaced/repaired or can be set to operate further. We also use two other NDT methods (AE and IRT) for comparison and validation.

2 Materials and Methods

The basic concept of our experimental methodology is shown in Table 1, which introduces the chronology of the different steps from manufacturing to the last test. First of all, we need to check the sensitivity of the DIC method for the identification of the presence, localization, and size of BVID in composite structures. Next, we need to compare the results

obtained by DIC methods with the results delivered by AE and IRT and show if the DIC method is more effective in examining BVID than other NDT methods. Then we need to define a correlation between the strain fields obtained with the DIC method, with the mechanical properties obtained with the standard tensile test in the location where the sample is broken. A clear interrelationship between the DIC strain field and real mechanical properties will enable the evaluation of the integrity of an FRPC structure and the prediction of the failure of an FRPC in an early stage of BVID development.

2.1 Preparation of FRPC Specimens with Defects

2.1.1 Production of FRPC Specimens

We produced composite sheets by vacuum-assisted resin transfer molding (VARTM). We used the epoxy resin Araldite LY 1564 (Huntsman International LLC, Texas, USA) (viscosity: 1200—1400 mPa·s at 25 °C, epoxy equivalent: 5.8–6.05 Eq/kg) and the curing agent Aradur 3487 (viscosity: 30–70 mPa·s at 25 °C, amine value: 9.30–10.20 Eq/kg). The mixing ratio was 100:34 wt% based on the manufacturer's recommendation. We used unidirectional carbon fabric PX35FBUD0300 (Zoltek Zrt., Nergesújfalu, Hungary) with a surface weight of 309 g/m^2 as reinforcement. The FRPC sheet had the following stacking sequence: [0°/90°/ + 45°/-45°]$_s$, where "s" stands for symmetry. This quasi-isotropic architecture is commonly used in vehicle structures under complex loads.

After they were produced, the FRPC sheets were post-cured in a Heraeus UT 20 oven (Heraeus, Hanau, Germany) at 80 °C for 8 h. Then specimens of 240 mm x 80 mm were cut from the FRPC plates with a Mutronic Diadisc (Mutronic, Rieden am Forggensee, Germany) diamond disc cutter. Ten specimens were prepared in this way.

2.1.2 Creation of Damage in FRPC Specimens

To create damage in the middle of the specimens, we used a Ceast Fractovis 9350 (Instron/Ceast, Torino, Italy) instrumented falling weight impact tester equipped with a 20 mm

Table 2 Designation of specimens, parameters of falling weight test, and visual characteristics of the damage created

Specimens	Falling weight test			Visual signs of defect	
	Impact energy, J	Drop height, mm	Impact velocity, m/s	Front side	Back side
S1	25	471.2	3.04	~ Ø10 mm contact mark & ~ 10 mm crack	~ 40 mm crack
S2	20	377	2.72	~ Ø10 mm contact mark	~ 30 mm crack
S3				~ Ø10 mm contact mark	~ 25 mm crack
S4	15	282.7	2.36	~ Ø10 mm contact mark	~ 20 mm crack
S5				~ Ø5-10 mm contact mark	~ 20 mm crack
S6	13	245	2.19	< Ø5 mm contact mark	~ 10 mm crack
S7				No visual damage	~ 10 mm crack
S8	10	188.5	1.92	No visual damage	No visual damage
S9				No visual damage	No visual damage
S10	0	–	–	No visual damage	No visual damage

Table 3 Characteristic forms of damage

	S1 (25J)	S2 (20J)	S4 (15J)	S6 (13J)	S8 (10J)	S10 (REF)
Front side						
Back side						
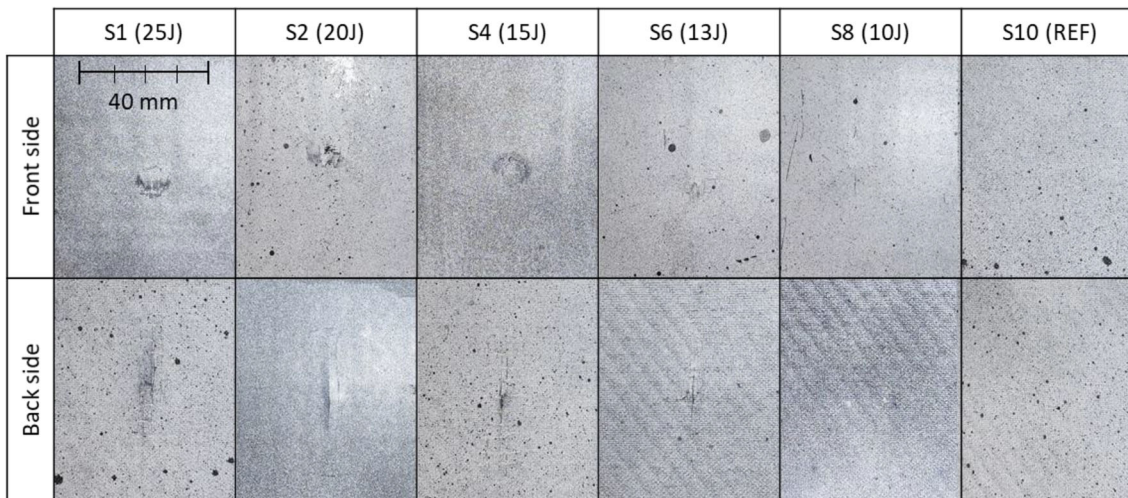
diameter sphere-ended dart. Different degrees of BVID were produced in samples with various impact energies from 10 to 25 J with 5 J steps (Table 2). The total drop weight used was 5.41 kg. We changed impact energy by changing the drop height. A maximum impact energy of 25 J was chosen as a maximum in our experiment, as it is the load limit under which the damage cannot be recognized easily on the front side of a specimen. At impact energy of 15 J, small contact marks on the front side of the specimen and short cracks along the back side of the specimen appeared. At 10 J, there were no visible defects. Based on this observation, the minimum impact energy which causes visually observable defects should be between 10 and 15 J. Therefore, we conducted extra experiments and found that the minimum impact load which can cause visual defects is 13 J. In Table 2, we summarised the visible marks on the specimens that were

hit with different impact energies. The specimens that were hit with a load between 13 and 25 J showed hair-thin cracks along the length of the reinforcement on the back sides of the specimens. These were matrix cracks between rovings in the outer layers. Table 3 visually presents the characteristics of different damages.

Next, we attached tabs to both ends of the specimens and painted the FRPC specimens with black and white spray in a random pattern to ensure sufficient contrast for DIC.

2.2 Experiments

2.2.1 Mechanical Test with DIC Test (Stage 1)

Tensile tests were conducted at room temperature with a Zwick Z250 universal testing machine (Zwick, Ulm, Germany). Tests were performed in displacement control, where the loading rate was 1.5 mm/min. The displacement limit was 0.15%, which was computed based on strain values from the connected Mercury Monet (Sobriety, Kurim, Czech Republic) optical strain measuring system (DIC). The gauge length for this global strain measurement was 100 mm. The free length of the specimens was 160 mm.

The experimental setup of DIC (Fig. 4a) included: two 5 MPixel resolution IDS U3-3080CP-P-GL (Imaging Development Systems Inc., Obersulm, Germany) cameras and two LED lights mounted on tripods. One camera and one LED light were mounted facing each side of the tested specimen to monitor both sides simultaneously. The distance between the cameras and the surfaces of the specimen was 340 mm. We used lenses with a focal length of 25 mm on both cameras. The results were recorded and processed with the Mercury RT-v2.6 software. The data were collected with a frame rate of 10 Hz.

Before the test, we calibrated the optical strain measurement system to avoid lens distortion and to correlate the real size of the specimen with its size in the recorded images. One pixel in the image was set equal to 0.194 mm in real size. The region of interest (RoI) shows the area where the strain field map was generated by DIC, and the strain values of the tested sample were measured by the line probe. Both the strain field map and the line probe were defined in the software (Fig. 4b). In the strain field, the calculated points were 20 pixels from each other, and the facet window size was 45 pixels × 45 pixels. In all cases, 0.2 confidence interval, high correlation quality, fast speed and full affine transformation were set up in the Mercury RT-v2.6 software. The default value of 0.2 confidence interval means that the found point is located within ± 0.2 px within the computed location with the 95% probability. Correlation quality specifies the interpolation method used in correlation. More complex methods are slower. Fast speed means the method searches in the intermediate neighborhood (Normal speed searches in

the whole image). The affine transformation type contains all three transformation types (translate, scale and shear).

2.2.2 Infrared Thermography (IRT)

We localized and analyzed the failures in the specimens by IRT with a FLIR A325sc (FLIR Systems, Wilsonville, USA) infrared camera (Fig. 5a). IRT was calibrated with the camera-object distance of 300 mm, a room temperature of 24 °C, and a humidity of 50%. The reflected temperature and emissivity were 24.3 °C and 0.95, respectively. The specimens were heated up to 75 °C in a Heraeus UT 20 (Heraeus, Hanau, Germany) oven before IRT. This temperature is low enough and has no adverse effects on the polymer matrix based on preliminary DSC and DMA tests. The IRT data were collected with a frame rate of 5 Hz. FLIR researchIR software was used to collect and analyze the data.

To make the results obtained for various samples comparable, we made the following assumptions:

1. In the FLIR camera software, we choose a reference area on the undamaged part of a specimen. The temperature of the reference area was used as the temperature of a specimen.

2. We analyzed the temperature field dynamics for the surface of the sample with the defect while the temperature of the reference area cooled from 70 °C to 30 °C.

3. We set up a sampling line across the defect and analyzed the temperature distribution along this line at certain moments of time. The obtained temperatures were regarded as the temperatures of the defects (Fig. 5b).

Since the BVID defect is not the same across the thickness, we needed to record the temperature dynamics for both sides of the specimen. Therefore, before examining the second surface, the samples were heated in the oven up to 75 ºC.

2.2.3 *DIC (Stage 2) + AE*

After the 80 mm wide specimens (S1–S10) were tested with DIC and IRT methods, they were further cut into 25 mm wide specimens. Thereby from one 240 × 80 mm FRPC specimen, we cut three specimens with the sizes 240 × 25 mm, which are the standard sizes for specimens used in tensile tests (Fig. 6). In such a way, we obtained one specimen with the damage in the middle and two specimens where the internal damage can possibly but not necessarily exist.

We tested the obtained specimens by DIC. The DIC setup and its settings are identical to the settings described in Subchapter 2.2.1. Additionally, in this experiment, we added AE to compare the results obtained by the DIC method with those delivered by the AE method and to prove that the applied load was still in the NDT range of the specimens. The AE microphones were mounted on the specimen by plastic clips. The AE signals were recorded by a Sensophone AEPC-40/4 (Gereb es Tarsa Ltd., Budapest, Hungary) device with

Fig. 4 **a** The DIC experimental setup, **b** schematic representation of a specimen (rotated by 90° compared to a))
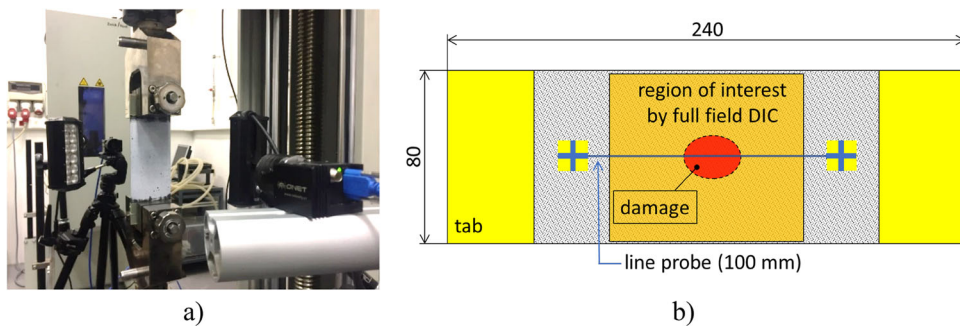

Fig. 5 **a** The setup of IRT, **b** schematic representation of the specimen
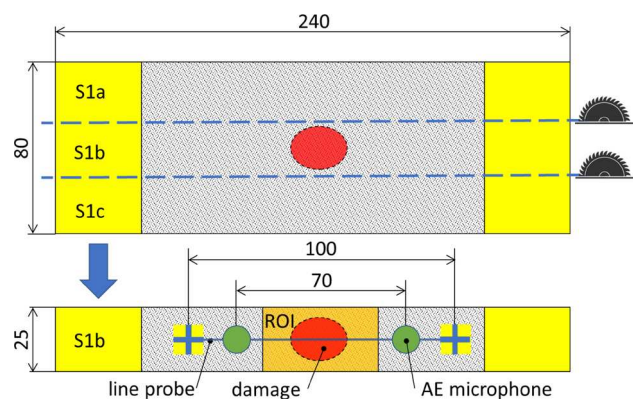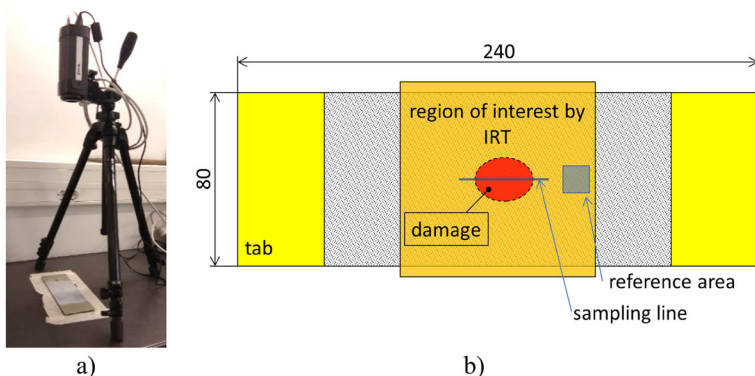

Fig. 6 Preparation of 25 mm wide specimens and their test setup

two Micros30s (Physical Acoustic Corporation, Princeton Junction, USA, operating frequency range: 150–400 kHz) microphones placed on the surface of the specimens. The distance between the microphones was 70 mm (Fig. 6), the coupling agent was Oxett silicon grease (T-silox Ltd., Budapest, Hungary), and the threshold was 20 dB (preliminary tests showed that the signals from crosshead movement did not give hits above this threshold), dead time was 5 ms, and the average sound velocity was 1400 m/s.

2.2.4 DIC (Stage 3)

In the last stage (Stage 3), the same parameters and setup were used, but the maximal elongation limit was switched

off, and the specimens were pulled until failure. The goal of this stage was to analyze the correlation between the ultimate strength and the structural integrity, which was predicted in the previous stage.

3 Results and Discussion

3.1 Infrared Thermography

We examined both sides of the samples by IRT to detect the damage. From the IRT test, we obtained the temperature field distribution on the surface of the sample. The temperature of the defect zone is usually lower than the temperature of undamaged parts. It is because of the larger free surface in the case of cracks and because of the delamination of layers. The surface layer is thin and cools faster, and the inner layer cannot replenish the heat on the visible surface so quickly because of the hindered heat transfer.

A significant difference was found in damage detectability for the two sides of the same specimens. The diagrams in Fig. 7 show the temperature distribution along the sampling line when the temperature of the reference area is 70 °C. The lower peaks of the temperature curves identify where the defect is localized. For the defects created with an impact energy of 20 and 25 J, we can observe clear peaks of the temperature curves for the front side of the samples (Fig. 7a). For damage created with an impact energy lower than 20 J, the

Fig. 7 Localizability of different levels of BVID on the front side (**a**) and the back side (**b**) by IRT
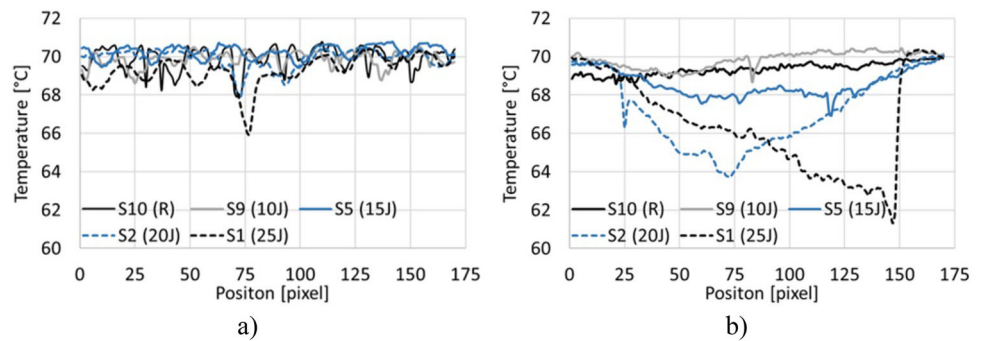
peaks of the related temperature curves are almost invisible. On the back of the specimens, the damage created with 15–25 J is clearly visible, and even 10 J damage can be detected if the sampling line is placed carefully (Fig. 7b). The main reason for this difference comes from the nature of BVID. The front side, where the tip of the falling dart hit the specimen, received a compression load, which can deform or even crack the matrix, but it does not significantly influence the IRT image. Contrary to this, the back side of the specimen deforms much more than the front side due to the tension caused by the falling weight. Therefore, the back side of the sample can exhibit fractured rovings and/or delamination between layers. We found out that above a critical impact energy, which was 15 J in this test, an open crack appeared on the back side of the specimens. Open damage has a higher free surface and, therefore, can cool down faster than the undamaged parts of the specimen. This is why it shows cooler spots in the temperature map.

The deviation of the temperature curves which belong to the front side of the samples (Fig. 7a) originated from the characteristics of the manufacturing process. Surface irregularities cause changes in temperature, which IRT shows. Moreover, IRT is sensitive to environmental conditions, which can cause asymmetric cooling. Figure 8a shows the temperature curves from both sides of the S10 reference specimen, where we can see the effect of surface irregularities and asymmetrical cooling, which are illustrated with the deviation and incline of temperature curves. Figure 8b shows a position of a sampling line and reference widow on an S1 specimen's back side. In fact, the position of the virtual sensor, which depends on the operator, also greatly influences the results.

We also examined the influence of the different reference temperatures on the IRT results. While the sample was cooling down, we recorded the IRT results for different reference temperatures and analyzed the sensitivity of the IRT method as a function of temperature. We found that lower temperature makes it more difficult to detect damage (Fig. 9a. To characterize the effectiveness of the IRT method at different reference temperatures, we used the following formula:

$$\mu_{IRT} = \frac{T_{ref} - T_{min}}{T_{ref}} \times 100[\%] \tag{1}$$

where μ_{IRT} is the coefficient of effectiveness of IRT, T_{ref} is the reference temperature of the sample, T_{min} is the minimum temperature on the sampling line. We summarized the results of the effectiveness of IRT in Fig. 9b. We observed that the lower the reference temperature, the worse IRT can localize the defect in a composite. These numerical values are particularly important because they are required when automated evaluation is programmed.

In sum, IRT is sensitive to the surface topology of the examined object, environmental conditions, the temperature of the inspected object, and the experience of the operator who performs the examination. Therefore, we can conclude that IRT cannot deliver accurate results for the NDT of composites in many cases. Moreover, IRT only provides visual identification of the defect, but the residual mechanical properties of the damaged composite cannot be characterized.

3.2 Connected Mechanical and DIC Test (Stage 1)

Extending the mechanical test with DIC is quite common practice, as such a combination provides a more accurate measurement of elongation and also, can provide images of the strain field of a structure under load. Defects of the structure (internal and external) cause inhomogeneity in the strain map, that is why DIC can clearly identify defects. A typical principal strain map of a damaged specimen delivered by DIC is presented in Fig. 10a. A strain concentration can be seen in the middle of the sample, which identifies the BVID. The analysis of the strain distribution shows that the roving which goes across the BVID has lower strain (inactive areas) compared to the other parts of the sample, which means that it is either partially or fully broken and does not carry a load. We also observed two spots with higher strain (active areas) next to the BVID, which demonstrates the so-called "bridge effect" when the nearest rovings take the load instead of the broken one.

Fig. 8 a temperature distribution of the both sides of the reference specimen at 70 °C **b** field of view of IRT and the position of sampling line and window
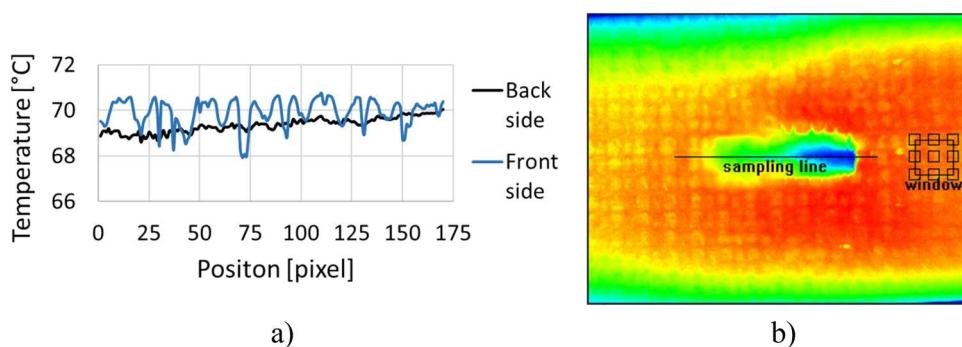

Fig. 9 a graphical and **b** specific representation of localizability reduction at different reference temperatures
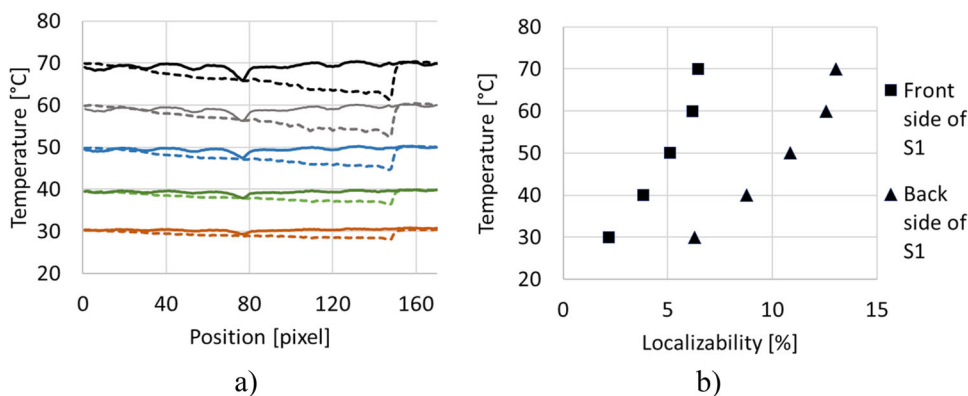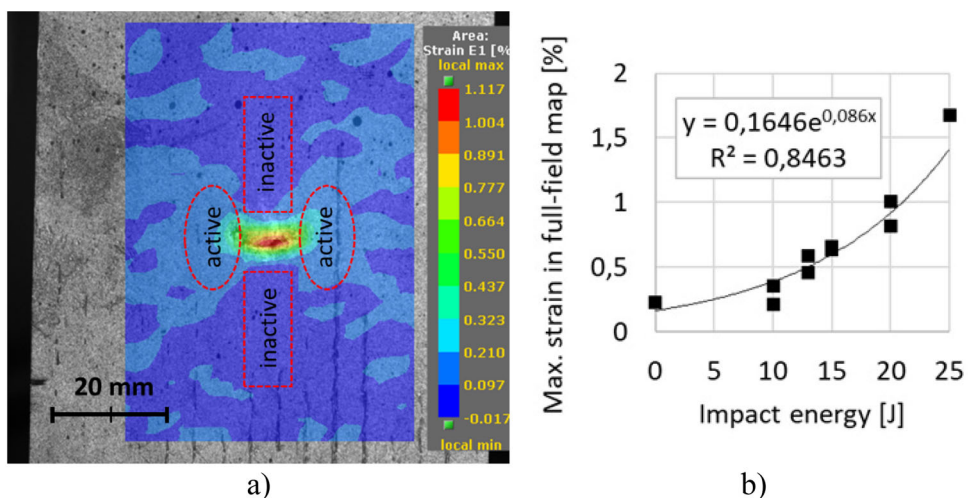

Fig. 10 A typical principal strain map of the composite sample under load (**a**) and the dependency of the maximum strain in the map on the impact load that created the damage (**b**)

We examined the samples under tensile load by DIC. We didn't break the specimens in this phase. We only loaded them to the strain limit of 0.15% and built a correlation between the maximum principal strain observed with full-field DIC and the impact load, which was used to create the damage (Fig. 10b).

Next, we examined the progressive behavior of damaged samples during tensile loading. We characterized their behavior with the progression of minimum, maximum, and average principal strains (ε_{min}, ε_{max}, and ε_{av} correspondingly) extracted from the strain maps. For the purpose of comparison, we also examined a sample without damage (hereafter, "reference sample" or S10). We found that for the reference sample, the progression of ε_{min} and ε_{max}, is symmetric to ε_{av} (Fig. 11a), and the standard deviations of the measured values are around 0.1% strain. Contrary to this, the distribution of ε_{min} and ε_{max} for the samples with the defects (S5 and S1) is asymmetric to ε_{av} (Fig. 11b, c). The difference between ε_{max} and ε_{av} increases with the size of the defect. Thus, the diagram of S1 (25 J) shows a very high strain compared to the average.

Furthermore, we defined new indicators, X and Y, which we used to compare the specimens. The value of X is the difference between the maximum and the average strain in the
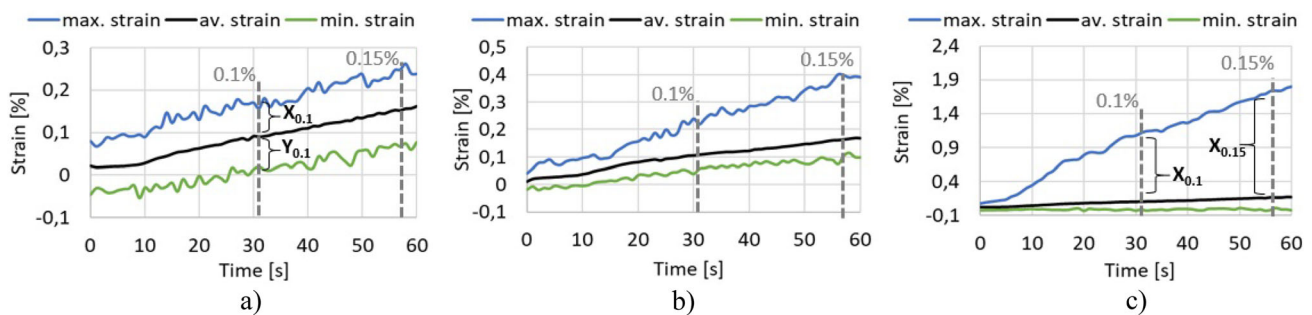
Fig. 11 Strain curves of specimens from the DIC full-field map **a** S10, **b** S5, **c** S1

full-field strain map at the moment defined by the average strain of the specimen. For example, $X_{0.1}$ means the difference between the maximum and average strain when the average is 0.1% (Fig. 11a). In a similar way, Y is the difference between the minimum and the average strain in the full-field strain map at the same moment.

Figure 12a shows the correlation between the presented $X_{0.15}$ value and the impact energy on both sides of the specimens. This diagram shows that the damage is detectable on the front side from 10 J impact energy, although the X values from the back side are close to the references. In the case of 20 and 25 J impact energy, the X values indicate the damage with similar efficiency on both sides. In a future test, this diagram can help us to predict easily how big the impact energy which damaged the examined object was.

Figure 12b shows the effect of the different strains on the indicators. The values of the indicator significantly increased when the load on the specimen was increased by 0.05%. It also means that the increasing load makes it possible to find a smaller defect in the structure. However, the test range should be kept quasi-non-destructive, so a control method is needed which can define a limit to our tensile test. It seems logical to choose AE for this.

It can be useful, but the main question of the periodic checking of expensive composite parts in the industry is how the damage influences the integrity of the structure. In the next stages, we will continue investigating this question.

3.3 DIC Testing (stage 2)

In the second stage of DIC testing, we cut the S1-S10 specimens further and retested the new, narrow pieces (25 mm wide) to learn more about damage development under load. Hence, we can compare the two pieces which originated from the sides of the old specimen with the specimens that come from the middle of the old specimen.

Figure 13 shows the strain maps of specimens S1a, S1b, and S1c when the total strain of the specimens was 0,1%. The S1b specimen, with the 25 J impact damage, shows a significantly different pattern in the strain map than the others. The

background of the strain map of S1b is mainly blue (~ 0.07%), which means that most of the specimen has very low strain compared to the damaged area, which is marked with yellow and red (~ 0.7–0.9%). This pattern does not change during the test, only the strain increases. S1a and S1c look like a usual reference specimen: green base (~ 0,1%) with random, continuously changing red and blue spots. It means that the specimen has an average strain with small locations that are overstretched or understretched. The strain curves can show more details, just like in the case of wide specimens. S1a shows continuously increasing strain, but the deviation and the symmetry indicate an undamaged structure, unlike S1b, where the maximum strain is much higher and continuously grows with the loading of the specimen. The strain field of specimen S1c is similar to that of S1a, but in the case of S1c, an alternation of maximum and minimum values can be observed on the curves. It comes from the red rectangular area of S1c, which shows the delamination in the specimen. At first, this area starts to show significant activity because of the load. Then most probably, the friction between the delaminated surfaces stops the further elongation of this part, so other undamaged parts start to activate, in other words, produce greater strain. When the elongation of the undamaged part reaches a critical point, the friction between delaminated layers ceases, and it presents high activity again. The falling weight generated this delamination, and the delamination spread to S1c from S1b. It is observable from the strain fields of S1b (red rectangles).

Investigation of the X values of the narrow specimens can help us to evaluate the level of damage in different parts of the wide specimens. We found that the samples from the sides were not damaged at all in the majority of cases. Therefore, during the investigation of DIC stage 1, these side parts carry the load of the damaged area. The narrow specimen from the middle with the damage can have higher X values without the undamaged side parts. With this data, we can investigate the ability of the method to detect BVID in composite samples with various ratios of damage. The damage surrounded by undamaged zones shows an $X_{0.1}$ value 50% lower than when the damage extends along the entire specimen width.

Fig. 12 a Indicators $X_{0.15}$ and $Y_{0.15}$ from both sides of the specimens which characterize the damages caused by different impact energy, **b** comparison of indicators X and Y obtained at different load levels
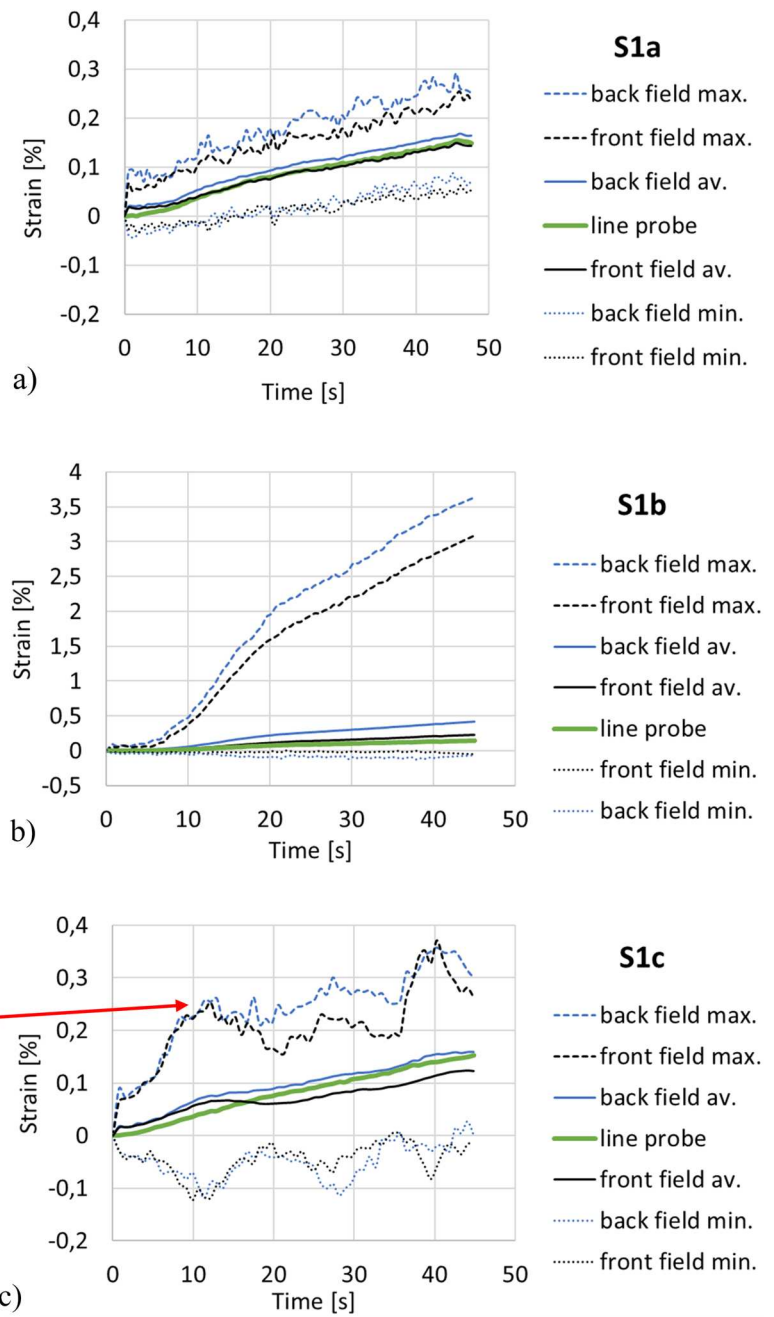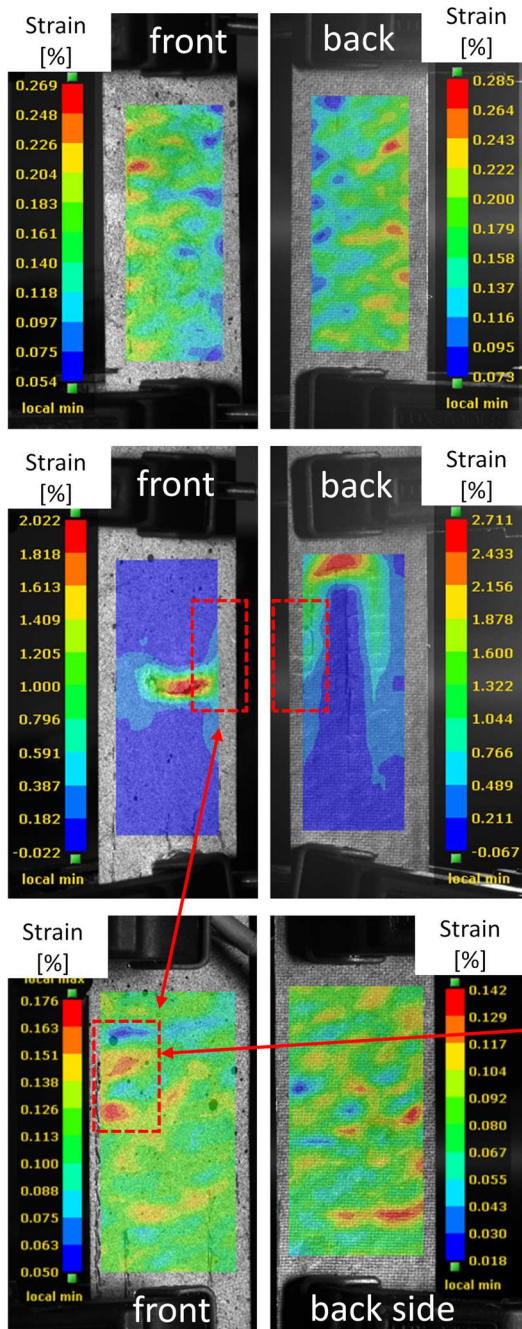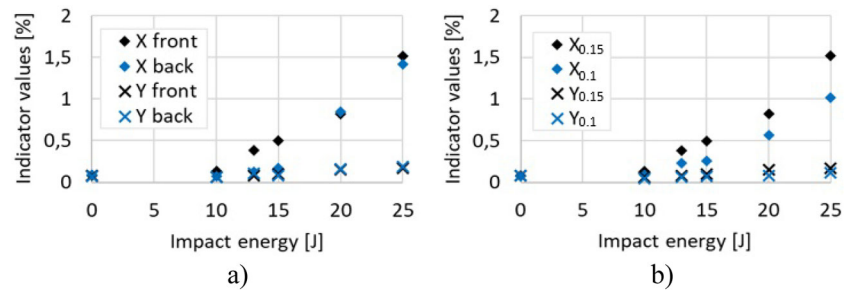

Fig. 13 Strain full-field maps and strain curves of specimens **a** S1a, **b** S1b (25 J), **c** S1c

AE monitoring was also used for collecting the data during the DIC examination of narrow specimens. We found that the applied tensile load, which caused a strain of 0.15% in the samples, can be safely considered non-destructive, because we can observe only 10–30 events for each test, which is negligible in the case of composites. In fact, when the composite structure is damaged, or damage is progressing, it generates a lot of AE events. To localize the origin of events, we used histogram representation with 5 mm steps. We found that based on only the AE histograms, it is not possible to clearly detect the damage with this small load. If a greater load were applied, a higher number of events can be observed, and damage could be localized clearly. However, it also would mean the test is not non-destructive anymore.

The obtained frequency and amplitude values of AE events collected during the reference specimen's tensile tests did not show significant differences compared to the data collected during tensile tests of the impacted specimens. Therefore, AE provides little information about the damage and does not show what happened to the specimens. However, DIC can easily show the active zones of the specimen where the events come from (Fig. 14). In the case of S1b, the different peaks originated from different sides of the specimen.

3.4 DIC testing (stage 3)

In stage 3, we performed tensile tests to characterize the remaining mechanical properties of the specimens. The stress–strain curves (Fig. 15a) show that specimens from the sides (S1a, S3a, S6a) can present the same or even higher ultimate strength and elongation than the reference specimen (S10 a). Note that specimens from the other side indicated with c show the same trend. It confirms that the sides of specimens (a, c) remained intact after the applied impact load. Opposite to this, specimens with b in the name from the middle showed significantly lower ultimate strength and strain.

Averaging the values of strength of the reference specimens and of the undamaged specimens from the sides indicated with (a) and (c), we determined the reference ultimate strength. This reference strength was used for the calculation of the strength reduction of damaged specimens. Specimens with 10, 13, 15, 20, and 25 J impact damage show approximately 10, 37, 40, 50, and 65% reduction in ultimate strength, respectively.

The X value of specimens grows exponentially with the reduction of ultimate strength (Fig. 15b). This diagram also shows that a higher tensile load ensures better correlation.

By defining the correlation between the reduction of strength and X, we achieved the goal of this experiment. Hence, we can present a DIC-based NDT method for evaluating the integrity of composite structures. Moreover, the reduction of the strength of the damaged area is predictable,

and the obtained results can be used as input parameters for FEA.

Therefore, finally, we proved our theory, which states that the reduction of strength is predictable from the surface strain field obtained by DIC for the examined composite structure with a certain combination of materials, stacking sequence, etc. All the other combinations require a new measurement and building their own relevant correlations. With this knowledge, companies can use the proposed method for the periodic inspection of their composite products and the estimation of the severity of the detected damage.

4 Summary and Conclusions

Our goal was to demonstrate the applicability of our new NDT-DIC method and reach a higher level of SHM in the case of BVID evaluation compared to traditional DIC method. The main difference between the existing DIC methods and the NDT-DIC is the extent of the applied test load which in the case of the NDT-DIC must be provably quasi-non-destructive. For this purpose, it is necessary to make preliminary test with the examined material and stacking sequence combination. This can be supplemented by obtaining the strain data of artificially damaged specimens, which gives the opportunity to estimate the residual strength values during a subsequent NDT-DIC test.

In stage 1, the artificially created damage was detected from the local inhomogeneity of strain fields. A pattern that is constantly changing under load indicates great structural integrity. On the other hand, a stable pattern indicates a defect. Such a pattern also indicates the mechanical effect of the damage in an indirect way. We found that the higher the maximum value in the strain field is, the greater the damage is in the structure. On both sides of the specimen, the defect is detectable by NDT-DIC. In addition to the patterns of the strain field, we investigated the maximum, average, and minimum strain–test time curves as well. We found that in the case of undamaged specimens, the maximum and minimum values increased together with the average values, and the strain differences from the average were roughly the same and low. In the case of damaged specimens, the maximum and minimum strain values changed asymmetrically compared to the average. We defined a new indicator (X) to characterize this effect, which shows the difference between the maximum and average strain values at a given moment. X can indicate the existence of damage. We presented a correlation between the value of the X indicator and impact energy.

The IRT examination of specimens, which was used as a reference for our primary NDT-DIC method, also successfully indicated damage on the back sides of the specimens, but it was much less sensitive to damage on the surface which was hit. Unfortunately, in most cases, the back sides of

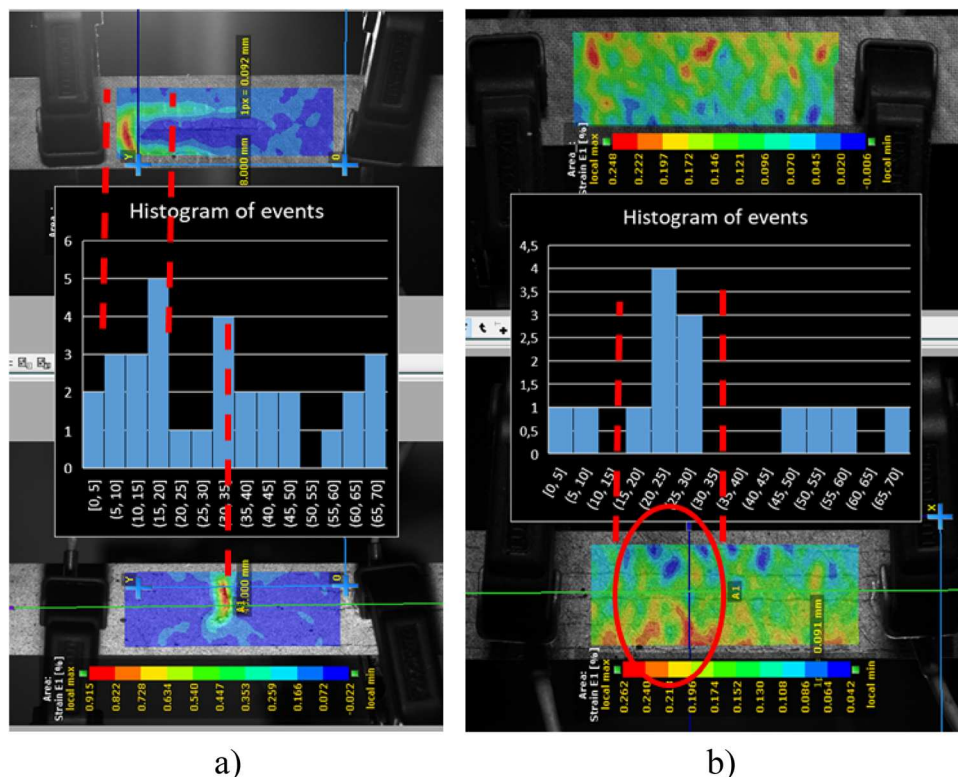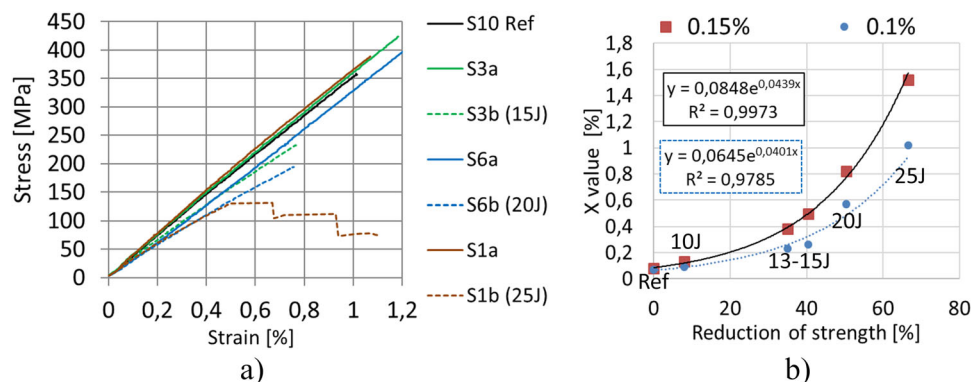**Fig. 14** AE linear localization of **a** S1b (25 J), **b** S10a (ref) specimens

Fig. 15 Results of tensile tests (**a**) and the final correlation between X and the reduction of ultimate strength (**b**)

structures are usually not accessible for testing. Furthermore, the IRT could not provide information about the mechanical effect of damage, so prediction of the remaining strength is impossible. Opposite to this, the NDT-DIC does not suffer from these two serious disadvantages. Based on this comparison, the novel DIC-based method can be a more advanced solution for the periodic quality control of FRPC structures. After cutting the specimens further, in stage 2, the NDT test proved that the side parts of the wide specimens had not been damaged during the falling weight test. These undamaged parts can partially hide the damage in the strain field of the first DIC test—after cutting the specimen into narrower parts, the detectability of damage was doubled in the narrow specimens. Our AE results suggest that a strain of 0.15% does not damage the specimen.

The ultimate strength of specimens was obtained with a tensile test. We found a strong correlation between X from the first DIC test and ultimate strength reduction. Based on our method, the complete evaluation (position, area, severity) of any BVID is possible with the non-destructive DIC test in the future in a certain combination of materials and stacking sequence.

Our future plan is to use the location, dimensions of BVID, and the remaining strength of the damaged part as input parameters for FEA, which will provide a reliable indication of structural damage.

Data Availability The raw/processed data required to reproduce these findings cannot be shared at this time due to technical or time limitations. Please contact the corresponding author for further assistance.

Declarations

Conflict of interest The authors declare that they have no known competing financial interests or personal relationships that could have appeared to influence the work reported in this paper.

Ethical Approval Not applicable.

Consent to Participate Not applicable.

Consent for Publication Not applicable.

References

1. Towsyfyan, H., Biguri, A., Boardman, R., Blumensath, T.: Successes and challenges in non-destructive testing of aircraft composite structures. Chin. J. Aeronaut. **33**(3), 771–791 (2020). https://doi.org/10.1016/j.cja.2019.09.017

2. Talreja, R., Phan, N.: Assessment of damage tolerance approaches for composite aircraft with focus on barely visible impact damage. Compos. Struct. **219**, 1–7 (2019). https://doi.org/10.1016/j.compstruct.2019.03.052

3. Szabó, F., Takács, L.: Experimental and numerical failure analysis of adhesive joint of glass fiber reinforced polymer composite. Period. Polytech. Mech. Eng. **64**(1), 88–95 (2019). https://doi.org/10.3311/PPme.15106

4. Bouhamida, B., Merzoug, A.: Novel analytical model of stress concentration around broken fibers of unidirectional composite plate. Period. Polytech. Mech. Eng. **65**(2), 120–128 (2021). https://doi.org/10.3311/PPme.16062

5. Rocha, H., Semprimoschnig, C., Nunes, J.P.: Sensors for process and structural health monitoring of aerospace composites: a review. Eng. Struct. (2021). https://doi.org/10.1016/j.engstruct.2021.112231

6. Wronkowicz-Katunin, A., Katunin, A., Dragan, K.: Reconstruction of barely visible impact damage in composite structures based on non-destructive evaluation results. Sensors. **19**, 4629 (2019). https://doi.org/10.3390/s19214629

7. Lee, S.-H., Kim, H., Hang, S., Cheong, S.-K.: Interlaminar fracture toughness of composite laminates with CNT-enhanced nonwoven carbon tissue interleave. Compos. Sci. Technol. **73**, 1–8 (2012). https://doi.org/10.1016/j.compscitech.2012.09.011

8. Fakirov, S.: Polymer nanocomposites: Why their mechanical performance does not justify the expectation and a possible solution to the problem? Express Polym. Lett. **14**(5), 436–466 (2020). https://doi.org/10.3144/expresspolymlett.2020.36

9. Chow, W.S., Mohd Ishak, Z.A.: Smart polymer nanocomposites: a review. Express Polym. Lett. **14**(5), 416–435 (2020). https://doi.org/10.3144/expresspolymlett.2020.35

10. Marino, S.G., Czél, G.: Improving the performance of pseudo-ductile hybrid composites by film-interleaving. Compos. Part A: Appl. Sci. Manuf. (2021). https://doi.org/10.1016/j.compositesa.2020.106233

11. Fotouhi, M., Fuller, J., Longana, M., Jalalvand, M., Wisnom, M.R.: The high strain rate tension behaviour of pseudo-ductile high performance thin ply composites. Compos. Struct. **215**, 365–376 (2019). https://doi.org/10.1016/j.compstruct.2019.02.068

12. Szebenyi, G., Hliva, V., Magyar, B.: Development of interphase engineering techniques for the ductility improvement in CF/EP composites – Comparison of NDT methods for delamination localization. Mater. Today: Proc. **34**, 113–116 (2021). https://doi.org/10.1016/j.matpr.2020.01.403

13. Molnar, K., Kostakova, E., Meszaros, L.: The effect of needleless electrospun nanofibrous interleaves on mechanical properties of carbon fabrics/epoxy laminates. Express Polym. Lett. **8**(1), 62–72 (2014). https://doi.org/10.3144/expresspolymlett.2014.8

14. Saghafi, H., Fotouhi, M., Minak, G.: Improvement of the impact properties of composite laminates by means of nano-modification of the matrix—a review. Appl. Sci. **8**(12), 2406 (2018)

15. Saeedifar, M., Saghafi, H., Mohammadi, R., Zarouchas, D.: Temperature dependency of the toughening capability of electrospun PA66 nanofibers for carbon/epoxy laminates. Compos. Sci. Technol. **216**, 109061 (2021). https://doi.org/10.1016/j.compscitech.2021.109061

16. Cohades, A., Branfoot, C., Rae, S., Bond, I., Michaud, V.: Progress in self-healing fiber-reinforced polymer composites. Adv. Mater. Interfaces **5**(17), 1800177 (2018). https://doi.org/10.1002/admi.201800177

17. Kling, S., Czigány, T.: Damage detection and self-repair in hollow glass fiber fabric-reinforced epoxy composites via fiber filling. Compos. Sci. Technol. **99**, 82–88 (2014). https://doi.org/10.1016/j.compscitech.2014.05.020

18. Vermes, B., Czigány, T.: Development of microcapsules. Mater. Sci. Forum **885**, 31–35 (2017). https://doi.org/10.4028/www.scientific.net/MSF.885.31

19. Gomes, G.F., de Almeida, F.A., Ancelotti, A.C., da Cunha, S.S.: Inverse structural damage identification problem in CFRP lmainated plates using SFO algorithm based on strain fields. Eng. Comput. (2020). https://doi.org/10.1007/s00366-020-01027-6

20. Li, D., Zhou, J., Ou, J.: Damage, nondestructive evaluation and rehabilitation of FRP composite-RC structure: a review. Constr. Build. Mater. (2021). https://doi.org/10.1016/j.conbuildmat.2020.121551

21. Wang, B., Zhong, S., Lee, T.-L., Fancey, K.S., Mi, J.: Non-destructive testing and evaluation of composite materials/structures: a state-of-the-art review. Adv. Mech. Eng. (2020). https://doi.org/10.1177/1687814020913761

22. Nayak, D., Ramesh, V., Augustin, M.J., Gupta, N., Ramesh Kumar, M., Patil, C.M.: Laser Scanning based methodology for on-line detection of inclusion in prepreg based composite aircraft manufacturing. Mater. Today: Proc. **24**, 591–600 (2020). https://doi.org/10.1016/j.matpr.2020.04.313

23. Vas, L.M., Kocsis, Z., Czigány, T., Tamás, P., Romhány, G.: Novel evaluation method of acoustic emission data based on statistical fiber bundle cells. J. Compos. Mater. **53**(17), 2429–2446 (2019). https://doi.org/10.1177/0021998319826666

24. Saeedifar, M., Najafabadi, M.A., Zarouchas, D., Toudeshky, H.H., Jalalvand, M.: Barely visible impact damage assessment in laminated composites using acoustic emission. Compos. B Eng. **152**, 180–192 (2018). https://doi.org/10.1016/j.compositesb.2018.07.016

25. Loutas, T., Eleftheroglou, N., Zarouchas, D.: A data-driven probabilistic framework towards the in-situ prognostics of fatigue life of composites based on acoustic emission data. Compos. Struct. **161**, 522–529 (2017). https://doi.org/10.1016/j.compstruct.2016.10.109

26. Saeedifar, M., Zarouchas, D.: Damage characterization of laminated composites using acoustic emission: a review. Compos. Part B: Eng. **195**, 108039 (2020). https://doi.org/10.1016/j.compositesb.2020.108039

27. Szebényi, G., Blößl, Y., Hegedüs, G., Tábi, T., Czigany, T., Schledjewski, R.: Fatigue monitoring of flax fibre reinforced epoxy composites using integrated fibre-optical FBG sensors. Compos. Sci. Technol. (2020). https://doi.org/10.1016/j.compscitech.2020.108317

28. Swait, T.J., Jones, F.R., Hayes, S.A.: A practical structural health monitoring system for carbon fibre reinforced composite based on electrical resistance. Compos. Sci. Technol. **72**(13), 1515–1523 (2012). https://doi.org/10.1016/j.compscitech.2012.05.022

29. Forintos, N., Czigany, T.: Multifunctional application of carbon fiber reinforced polymer composites: electrical properties of the reinforcing carbon fibers–a short review. Compos. B Eng. **162**, 331–343 (2019)

30. Shahbaz, S.R., Berkalp, Ö.B., Zameer Ul Hassan, S., Siddiqui, M.S., Bangash, M.K.: Fabrication and analysis of integrated multifunctional MWCNTS sensors in glass fiber reinforced polymer composites. Compos. Struct. (2021). https://doi.org/10.1016/j.compstruct.2020.113527

31. Hegedus, G., Sarkadi, T., Czigany, T.: Self-sensing composite: reinforcing fiberglass bundle for damage detection. Compos. Part A: Appl. Sci. Manuf. (2020). https://doi.org/10.1016/j.compositesa.2020.105804

32. Caminero, M.A., Lopez-Pedrosa, M., Pinna, C., Soutis, C.: Damage assessment of composite structures using digital image correlation. Appl. Compos. Mater. **21**(1), 91–106 (2013). https://doi.org/10.1007/s10443-013-9352-5

33. Rao, J., Saini, A., Yang, J., Ratassepp, M., Fan, Z.: Ultrasonic imaging of irregularly shaped notches based on elastic reverse time migration. NDT & E Int. (2019). https://doi.org/10.1016/j.ndteint.2019.102135

34. Gresil, M., Poohsai, A., Chandarana, N.: Guided wave propagation and damage detection in composite pipes using piezoelectric sensors. Procedia Eng. **188**, 148–155 (2017). https://doi.org/10.1016/j.proeng.2017.04.468

35. Ricci, F., Monaco, E., Boffa, N.D., Maio, L., Memmolo, V.: Guided waves for structural health monitoring in composites: a review and implementation strategies. Prog. Aerosp. Sci. **129**, 100790 (2022). https://doi.org/10.1016/j.paerosci.2021.100790

36. Khechai, A., Tati, A., Guerira, B., Guettala, A., Mohite, P.M.: Strength degradation and stress analysis of composite plates with circular, square and rectangular notches using digital image correlation. Compos. Struct. **185**, 699–715 (2018). https://doi.org/10.1016/j.compstruct.2017.11.060

37. Szebényi G, Hliva V, Tamás-Bényei P (2019) Investigation of delaminated composites by DIC and AE methods. Twenty-second international conference on composite materials (ICCM22). Melbourne, Australia, 11–16 August 2019.